Engineering Geology 245 (2018) 248–257

Contents lists available at ScienceDirect

Engineering Geology

journal homepage: www.elsevier.com/locate/enggeo

Influence of environmental parameters on the seismic velocity changes in a clayey mudflow (Pont-Bourquin Landslide, Switzerland)

Grégory Bièvre[a,*], Martin Franz[b], Eric Larose[a], Simon Carrière[a], Denis Jongmans[a], Michel Jaboyedoff[b]

[a] Univ. Grenoble Alpes, Univ. Savoie Mont Blanc, CNRS, IRD, IFSTTAR, ISTerre, 38000 Grenoble, France
[b] Institut des Sciences de la Terre, Université de Lausanne, Lausanne 1015, Switzerland

ABSTRACT

An earthflow/mudflow of a few thousand cubic metres occurred at the toe of the Pont-Bourquin Landslide (PBL, Swiss Alps) in late August 2010. This event was preceded by a drop of about 6% in surface wave velocity (dV/V) determined from ambient vibration records. A seismic monitoring system made of three pairs of sensors was re-installed across the transportation and accumulation zones of the landslide in October 2011, allowing daily relative changes in seismic velocity to be measured for a period of 4.5 years. No similar drop in dV/V was observed during this period, consistently with the lack of significant landslide acceleration or earthflow/mudflow events. However, the three dV/V time series showed periodic and reversible variations in a range − 2% to 2%, suggesting a probable influence of seasonal parameters. They were cross-correlated to daily environmental (temperature and rainfall) and surface displacement time series. In the long term (yearly scale), dV/V variations are mainly driven by the temperature with short delays (30 to 50 days) indicating that the shallow layer (first 2 m) controls the dV/V variations. In the short term, the landslide response to precipitations exhibits a small decrease in dV/V with a delay of 2 to 5 days, in contrast with the displacement rate that almost instantaneously responds to the rainfall. The continuous seismic monitoring of PBL using ambient vibrations has proved to be a robust method for getting information at depth, with no data gap even during winters. The seasonal reversible seismic velocity variations turned out to be in a range lower than the drop observed before the August 2010 earthflow/mudflow, highlighting the interest of incorporating the dV/V technique in monitoring systems.

1. Introduction

Some landslide types, like rockfalls or mudflows, are a serious threat to the population, because of their suddenness which makes them difficult to predict. Except for their common suddenness, these two rapid mass movements exhibit distinctive characteristics, both for the sliding material (clay-rich formations for mudflows and rocks for rockfalls), their mechanisms (ductile rheology in clays, brittle behaviour in rocks) and their sensitivity to climatic conditions. In particular, the triggering or reactivation of mudflows and earthflows is strongly controlled by the hydro-meteorological conditions and water infiltration in the mass (Picarelli et al., 2004; Malet et al., 2005; Hungr et al., 2014). The forecast of these events and the search of precursors have been an active research topic for the last two decades. Precursors were sought by monitoring surface displacement and fissure opening and their evolution to rupture (Petley, 2004), or by using hydrological parameters, such as rainfall, pore water pressure and water content, associated with threshold values determined in an empirical or statistical way (Glade et al., 2000; Guzzetti, 2000; von Ruette et al., 2011). The application of these precursors, however, turned out to be very sensitive to the landslide characteristics and provide limited insights into the landslide dynamics. Physical models have then been developed to assess the effects of hydrological parameters on the triggering of rainfall-induced landslides (among others, Iverson et al., 2000; Simoni et al., 2008; Lu et al., 2010; Arnone et al., 2011). However, these models rarely considered the progressive deformation along the slope before landslide triggering (Fan et al., 2015).

In recent years, it has been shown that mechanical damaging can be monitored through the properties of ambient seismic noise that are an alternative to classical geotechnical tests (Del Gaudio et al., 2014; Larose et al., 2015). Indeed, the evolution with time of seismic noise properties (spectral amplitudes, frequency signature, spectral ratio amplitudes, and wave polarization) allows tracking variations of internal mass characteristics through different processing techniques. For fractured rock slopes, seismic noise studies showed that the ground motion is polarized and locally amplified at specific frequencies (Burjánek et al., 2010; Lévy et al., 2010; Burjánek et al., 2012; Bottelin et al., 2013a; Colombero et al., 2017; Valentin et al., 2017; Burjánek et al., 2018). In particular, noise measurements on a prone-to-fall column identified the resonance frequencies and showed the frequency decrease with the progressive decoupling of the column from the rock mass (Lévy et al., 2010). By contrast, reinforcement works on an

* Corresponding author.
E-mail address: gregory.bievre@univ-grenoble-alpes.fr (G. Bièvre).

https://doi.org/10.1016/j.enggeo.2018.08.013
Received 12 February 2018; Received in revised form 24 August 2018; Accepted 28 August 2018
Available online 05 September 2018

unstable limestone column provoked an increase in resonance frequencies resulting from the additional stiffness provided by the bolting (Bottelin et al., 2017). All the long-term seismic noise recordings detected significant reversible resonance frequency variations caused by meteorological fluctuations (mainly temperature but also thaw-freeze cycles), which have to be removed to characterize irreversible damaging or reinforcing effects (Bottelin et al., 2013b; Bottelin et al., 2017).

In clayey landslides, such as the large Avignonet landslide affecting a thick glacio-lacustrine layer in the Trièves areas (French Alps), it has been observed that the superficial shear wave velocity (*Vs*) significantly decreased with the material destructuration (Jongmans et al., 2009). As the mechanism of resonance in clayey landslides can arise from *Vs* contrasts resulting from landslide damaging or existing lithology (Méric et al., 2007; Jongmans et al., 2009), it turned out that the landslide effect is better tracked by changes in material seismic velocity (Renalier et al., 2010a). In the past decade, passive seismic has emerged as a new technique to retrieve the propagation characteristics between two receivers by cross-correlation of the time series (for a recent review, see Snieder and Larose, 2013). Indeed, it has been demonstrated both theoretically and experimentally that the cross-correlation of a diffuse wavefield recorded at two distant receivers converges toward the Green's function of the medium between these two receivers, assuming that the seismic noise is random (Shapiro and Campillo, 2004). This technique was first applied to the Avignonet landslide (French Alps) for both imaging and monitoring purposes (Renalier et al., 2010a, 2010b).

The first significant irreversible change in *Vs* was observed in the Pont Bourquin landslide (PBL; Swiss Alps; Fig. 1a,b) where a few thousand cubic metres earthslide-earthflow was triggered in August 2010 and evolved to a mudflow. The surface wave velocity measured over a 4-month period using seismic noise cross-correlations decreased continuously and rapidly for several days prior to the failure with a total relative drop *dV/V* of about 6% (Mainsant et al., 2012a). This drop was interpreted as resulting from a decrease in *Vs* at the base of the landslide (see the description of the landslide, Fig. 1c). This example illustrates the ability of ambient seismic noise to detect rigidity variations before landslide triggering. Over a longer measuring period of 3 years, Larose et al. (2015) pointed out seasonal fluctuations *dV/V* of +/− 2%, on the same site which they associated to meteorological fluctuations. However, terrestrial laser scanner and point geodetic measurements at the Pont-Bourquin landslide show continuous surface velocity of about 1 m/month (Mainsant et al., 2012b), raising the question of the relation between environmental, kinematics and *Vs* variations.

The objectives of the paper are twofold. The first objective is to put the failure of August 2010 back in the context of the global kinematics of the landslide and of the *dV/V* variations, which were recorded during a quiet 4.5-year period. The second objective is to investigate and quantify the relations between, one the one hand, the variations in *dV/V* at three different elevations along the slope, and, on the other hand, the geodetic data and the hydrometeorological parameters (temperature, rainfall and water table), benefiting from the continuous time series available on the site after the failure.

2. The Pont-Bourquin landslide

The Pont-Bourquin Landslide (PBL) is located 20 km to the east of Geneva Lake in the Swiss Prealps (Fig. 1a). It is approximately 240 m long and its width varies from 15 m to 60 m. The maximum depth is around 20 m and its average slope is around 25° facing south. The total volume of the landslide was estimated to be around $40 \times 10^3\,m^3$ but the most active part is around $11 \times 10^3\,m^3$ (Jaboyedoff et al., 2009). Numerous investigations have been carried out on PBL and only the main landslide characteristics are summarized here before presenting the conceptual mechanical model used for installing the monitoring system.

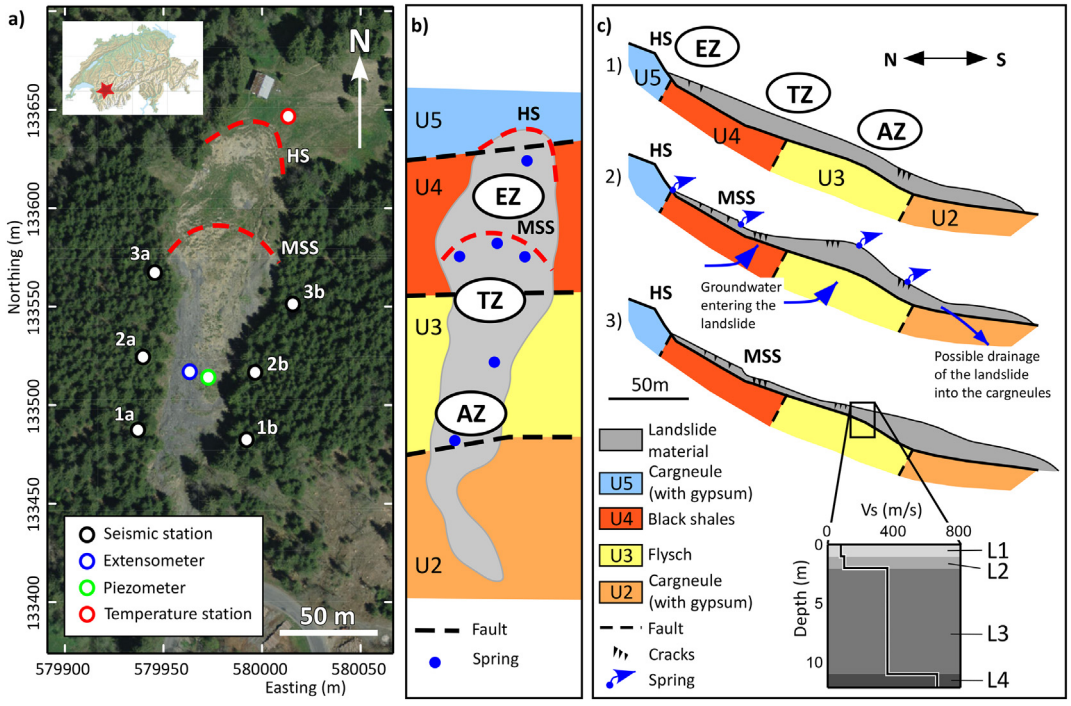

Fig. 1. a) Location of the study site and of the instruments on the slope. Coordinates are metric and expressed in the Swiss Grid format. HS: main headscarp; MSS: main secondary scarp. b) Simplified geological map with the location of springs and of the identified zones. EZ: erosion zone; TZ: transportation zone; AZ: accumulation zone. c) Conceptual model of the evolution of PBL showing 3 stages: 1) stable state, 2) landslide in the EZ with transportation of material to the AZ, 3) Triggering of a debris flow in the AZ after heavy rainfall. The *Vs* profile with the different interpreted units (L1 to L4) in the accumulation zone is shown (modified from Mainsant et al., 2012a).

2.1. Geology and hydrogeology of the PBL

The PBL crosses a complex geological zone made of five structural units (Badoux et al., 1990) separated by tectonic thrusts dipping approximately 35° toward the North. From the bottom to the top of the slope, the lithology is made of the following units (Jaboyedoff et al., 2009; Fig. 1b): (U1) weathered Triassic gypsum actively dissolved, not appearing on the map, (U2) > 50 m of Triassic cargneule (vacuolar dolomite) with a high permeability, (U3) approximatively 150 m of Flysch including thin beds of turbidites made of shale siltstone and few conglomeratic beds, (U4) 70 m-thick layer made of thin beds of Aalenian black shales, and (U5) another layer of cargneule. All these geological units are folded and faulted. Bedding measurements on units (3) and (4) revealed a general 35° dipping toward the North. The uppermost 3 m of these two units are furthermore affected by flexural toppling. Finally, units (4) and (5) are covered by quaternary moraines.

From a morphological point of view, the headscarp *HS* approximately coincides with the limit between the black shales and the cargneule. The landslide is affected by a main secondary scarp (*MSS*; Fig. 1) that is located over the limit between the black shales and the underlying flysch. In the upper part of the landslide (between *HS* and *MSS*) the black shales are continuously eroded, generating prone-to-move clayey material (Erosion Zone EZ). Below *MSS*, the material moves down regularly (Transportation Zone TZ) and accumulates in the lower part of the landslide (Accumulation Zone AZ).

This geological heterogeneity induces a complex hydrogeological setting, with at least 3 distinct groundwater flow regimes (Brönnimann, 2011). The upper part, composed of permeable vacuolar dolomite (cargneule) overlaid by low permeability moraines, is an aquifer where excess pore water pressure can develop, generating springs at the headscarp. The water of this aquifer can also percolate through the fractured black shale and flysch layer, creating springs along the secondary scarp and in the lower part of the landslide. Potentially, some inflow may also originate from the underlying bedrock. Finally, the lower permeable vacuolar dolomite (geological unit U2) contributes to drain the landslide. The presence of a perennial spring in the lower part of the landslide also suggests that a deeper groundwater source and path may exist in the slope, below the landslide.

The predisposing factors favouring the PBL are the following (see Jaboyedoff et al., 2009; Mainsant et al., 2012a for more details): (1) the weak bedrock such as black shales and flysches are prone to slope deformation; (2) the cargneule and gypsum units located at the toe of the landslide, which are highly soluble and deformable rocks, have most probably weakened the slope creating a lack of buttress at the toe; finally, (3) the chemical weathering and freeze-thaw cycles have contributed to a high degree of fragmentation of the outcropping rocks. As such, the PBL material is peculiar. It shows an evolution of its forming materials, starting with rocks (by contrast with soil material) or stiff clays and quickly evolving toward mud. The predominantly clayey moving mass is then made of a mixture of 1) weathered debris from the black shales transformed in mud, 2) morainic material and 3) flysch. The landslide is mostly translational and exhibits a slight rotational component at its top.

2.2. History of PBL

Orthophotos from 1995, 1997 and 2004 show a constant degradation caused by slope movements and erosion in the PBL area. Surface movements have been studied more carefully since 2006 when a scarp of 0.8 m was observed at the top of the landslide. On July 5th, 2007 a sudden earthflow of around 3–6 $\times 10^3$ m^3 cut the road joining Les Diablerets to Gstaad after 95 mm of rain in 3 days (Jaboyedoff et al., 2009; Mainsant et al., 2012a). In the following years, the landslide permanently moved and showed progressive retrogression at *HS* of a few metres per year. From 21 July to 23 August 2010, the landslide suddenly accelerated with movements reaching locally 21 m/month. This fast motion of material created a bulge at the toe of the landslide. In the meantime, sliding velocities at the head and the secondary scarps were lower than 0.5 m/month. On August 19th, 2010 this accumulation of material failed dramatically generating a mudflow that reached the river downhill.

2.3. Geophysical measurements

The landslide geometry was determined using longitudinal and transversal seismic and ERT (Electrical Resistivity Tomography) profiles (Mainsant et al., 2012a). The *Vs* profile measured by Mainsant et al. (2012a) at the top of the accumulation zone is shown in Fig. 1c. From top to bottom, three main seismic layers were found: (1) a 2 m thick shallow layer with a very low *Vs* of about 90 m/s, (2) a 9 m-thick layer with *Vs* = 360 m/s, and (3) the bedrock with *Vs* around 640 m/s, where is located the rupture surface. It was shown (Mainsant et al., 2012a) that *dV/V* variations in the frequency range 8–12 Hz could be influenced both by *Vs* variations in the shallow layer and in the 2 m thick layer at the base of the landslide (10 m in depth) where the rupture occurred.

2.4. PBL mechanism

Fig. 1c shows the conceptual model of the landslide derived from existing information and observation, and its evolution with time. In stage 1 the motion is initiated at the headscarp *HS* located at the top of the black shale layer. The sliding material is mainly made of the weathered black shale layer but the landslide also includes the weathered flysch layer. In stage 2, the main secondary scarp was created by the faster motion in the central transportation zone, probably resulting from the flow of water from below the landslide. The moving material accumulates in a bulge at the lower part of the landslide, steepening the slope and regularly generating mudflows or debris flows (stage 3). PBL is then a complex and composite landslide combining different types of movements (Hungr et al., 2014), which vary in space and time. In the upper part (erosion zone), it shows a solid behaviour at the main scarps where rotational sliding and toppling are observed. Most of the landslide is however translational in the transportation zone. Depending on its fragmentation and water content, the heterogeneous clayey material can behave mechanically in several ways, alternating superficial earthflows, debris flows and mudflows. The study of the August 2010 earthflow/mudflow event (Mainsant et al., 2012a) has suggested that the material obeyed a viscoplastic-type constitutive law (Herschel-Bulkley Model).

3. Methods

Meteorological, kinematics and geophysical data were acquired during the seismic monitoring period extending from October 2011 to March 2016. The characteristics of the available time series are given in Table 1.

3.1. Hydro-meteorological data

Environmental data were obtained from stations located on or nearby the study site. Temperature time series were measured at a

Table 1
Time extent of the cross-correlated time series.

Parameter	Start	End	Daily measurements available
Rainfall	01/10/11	15/04/16	1658
Temperature	25/10/11	15/10/15	1451
Extensometer	19/04/12	15/04/16	1248
Piezometer	05/07/10	29/05/14	432
Seismic velocity (*dV/V*)	25/10/11	15/03/16	1603

weather station installed on the upper part of the landslide (location in Fig. 1a). Hourly measurements were turned into daily values by calculating the average of the 24 values. Technical issues did not allow to use the rainfall data recorded at the weather station. Daily rainfall data were then provided by a station operated by the Federal Office of Meteorology and Climatology (MeteoSwiss) and located in the village of Les Diablerets, 500 m SW of the landslide. Piezometer data (location in Fig. 1a) were obtained from permanent pressure cells installed in a drilling at 4 m depth (December 2011 to February 2012) and at 2.35 m depth (November 2012 to mid-March 2014). Pressure measurements were compensated for atmospheric barometric pressure.

3.2. Landslide kinematics

An extensometer was installed to monitor surface displacements in the accumulation zone (Fig. 1a). Several gaps are present within the time series, which originate from the landslide activity, from snow and from falling trees.

Nine to twelve prism targets were installed within the unstable area, with one reference target installed on the stable zone. These targets were surveyed using a Topcon GPT-9003 M total station on a fixed base located 650 m south from the PBL, which provided the 3D positions of the targets. During the survey period (2010–2016), several targets had to be repositioned because they were damaged or displaced by the landslide activity, snow pushing, and sheep bullying. This led to a loss of continuity with a gap between Autumn 2012 and Spring 2013 when the whole set of targets had to be removed.

Topographic changes were also monitored using terrestrial laser scanner (TLS) surveys. The acquisitions were performed from the summit of a small hill located 650 m south of the PBL (same location as the total station base), allowing a survey of the upper part of the landslide. The TLS device was an Optech ILRIS-3D-ER using a laser with a wavelength of 1500 nm and with a maximum acquisition distance ranging from 800 m to 1200 m. Reduced acquisitions (2–3 scans) were performed approximately every 2 months during the snow-free seasons, and a full acquisition (10–15 scans) was conducted once a year. The point clouds were created by merging all the scans and a 4-step process was applied to the data (Franz et al., 2016). First, raw point clouds are manually filtered to remove dust, bugs, vegetation, *etc.*, using the Pifedit software (PolyWorks suite; www.innovmetric.com). Second, the coeval scans are co-registered. Third, the co-registered point clouds from different time series are aligned with each other, using vegetation-free ground assumed as stable outside the sliding area. This is done using the best-fit algorithm implemented in PolyWorks. Finally, the batch of co-aligned point clouds is georeferenced on a High-Resolution Digital Elevation Model (HRDEM) with a 0.3 m resolution (Rusinkiewicz and Levoy, 2001; Salvi et al., 2007) using CloudCompare (http://www.danielgm.net/cc/). This allowed the 3D reconstruction of georeferenced point clouds on the landslide whole surface and at different time steps. Using the shortest distance comparison method (implemented in CloudCompare) between two point clouds, it is possible to identify the morphological processes affecting the landslide.

3.3. Seismic monitoring

Three seismic sensors were installed on each stable flank of the slide and defined three pairs across the PBL (Fig. 1a). The two upper pairs (2a-2b and 3a-3b) are across the transportation zone while the lowest one (1a-1b) investigates the accumulation zone. The seismic sensors were vertical short period (2 Hz) velocimeters and ambient vibrations were recorded with a sampling frequency of 250 Hz. The vertical seismic noise field is mainly made of dispersive Rayleigh waves (Bonnefoy-Claudet et al., 2006) and the relative changes in Rayleigh wave velocity dV/V across the landslide were analysed using the ambient noise cross-correlation technique. Even if noise sources are not homogeneously spread around the landslide, Mainsant et al. (2012a) showed that daily cross-correlation allowed to reconstruct satisfyingly the Green's function since the seismic sources were relatively stable in time and space. The seismic noise primarily originates from the traffic on the road at the foot of the slide, and the reproducibility was good enough to guarantee stable daily correlograms (Hadziioannou et al., 2009). As such, this led to work with daily values of dV/V and, consequently, to further correlate them with daily values of environmental and displacement data. Hourly seismograms were first standardized (subtraction of the mean and normalization by the standard deviation of the dataset) to get seismic time-series with a mean centred on zero and with a variance of 1. Signals were then whitened between 4 and 25 Hz to give comparable statistical weight to each frequency. Data were then cross-correlated and a daily correlogram was determined between each couple of sensors (1a-1b, 2a-2b, and 3a-3b) by calculating the average of the 24 hourly correlograms. A reference correlogram was then set for each couple of sensors, corresponding to the mean of all daily correlograms. Daily velocity changes, with reference to the mean correlogram, were calculated using the stretching technique (Sens-Schönfelder and Wegler, 2006; Hadziioannou et al., 2009). This technique resamples the correlograms in time and the relative velocity change dV/V between a daily correlogram and the reference correlogram is taken as the one corresponding to the time shift for which the correlation coefficient cc is maximum.

Sensitivity tests (namely the calculation of the Power Spectral Density; see Appendix A) conducted between 4 Hz and 20 Hz showed that the highest correlation coefficients (above 0.9) were obtained between 8 Hz and 12 Hz. This confirms previous results by Mainsant et al. (2012a) who showed that this frequency range is the most stable and is adequate to monitor the landslide rigidity. Depth sensitivity kernels computed for three frequencies (8 Hz, 11 Hz and 14 Hz) showed that, for the *Vs* layering in the landslide, surface Rayleigh waves were sensitive to changes in the first two metres, as well as to changes at the bottom of the moving mass located at a depth of about 10 m (Mainsant et al., 2012a).

3.4. Cross-correlation between seismic, environmental and surface displacement time series

The linear relationships between relative seismic velocity changes and environmental data (air temperature and rainfall,) were further studied using cross-correlation. This mathematical technique is classically applied in hydrogeology, notably to study the linear dependency between rainfall and aquifer recharge (Larocque et al., 1998; Lee and Lee, 2000; Lee et al., 2006; Okkonen and Klove, 2010), providing quantitative information such as the correlation coefficient and the time lag. In landslide study, this technique has however been little applied. Helmstetter and Garambois (2010) used it on the Séchilienne rockslide (French Alps) to correlate seismic catalogues and environmental parameters (rainfall). They evidenced very short reaction times (< 1 day) between rainfall and the initiation of rockfalls and of micro-earthquakes within the landslide.

As for seismic data, time series were first standardized (all standardized time-series are presented in Appendix B) and were then cross-correlated with each other. The correlation of two functions f(t) and g(t) determines a lag t that is positive if g(t) leads f(t). The 95% confidence interval r, in this case, depends only on the length of the dataset (Diggle, 1990; Chatfield, 2003) and is classically of the form:

$$r = \frac{2}{\sqrt{n}} \quad (1)$$

where n is the length of the dataset. To further study the influence of long-term (seasonal) or short-term events on dV/V series, dataset were also high-pass and/or low-pass filtered prior to cross-correlating them, using a second-order Butterworth filter.

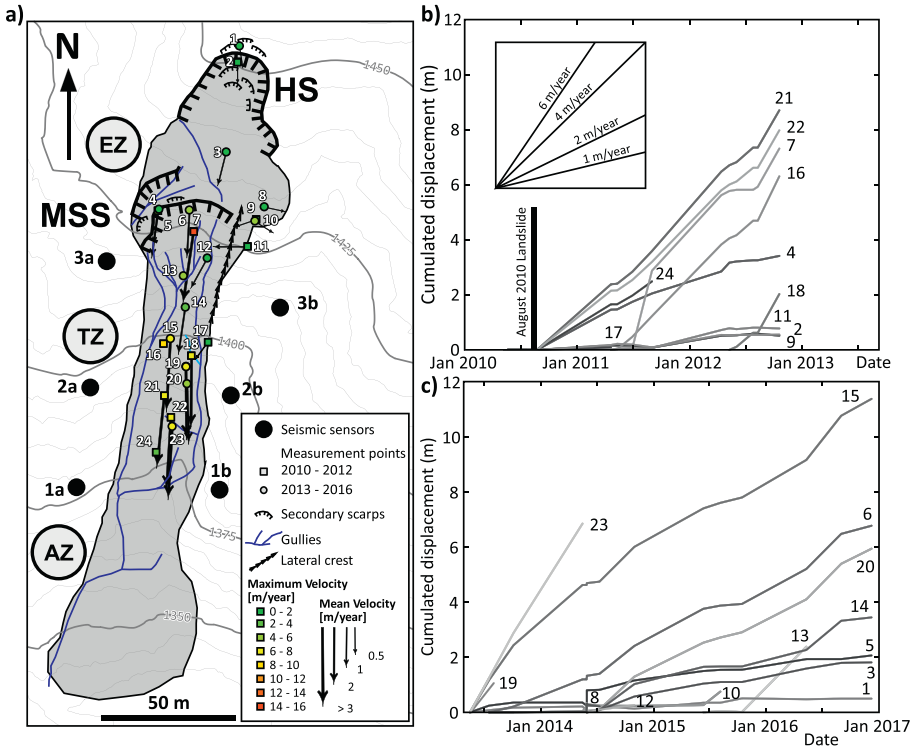

Fig. 2. Pont-Bourquin Landslide (PBL) kinematics. a) Velocities obtained with Total Station Survey. The squares represent the maximum velocities measured between August 2010 and October 2012 while the circles those between May 2013 and December 2016. The arrows illustrate the average velocities during the survey period of each point. The primary and the secondary scarps (HS and MSS, respectively) show moderate velocities whereas the central part (TZ) displays very high velocities. Note that the lower part (AZ) was not in the line of sight and thus does not have displacement rate measurement. b) and c) 3D total displacement vectors for periods 2010–2012 (squares in Fig. 2a) and 2013–2016 (circles in Fig. 2a), respectively. Same notations as in Fig. 1.

4. Results

4.1. Landslide kinematics

4.1.1. Total station – target tracking

The displacement rates measured by target tracking are shown on the landslide map in Fig. 2a, while the displacement-time curves are shown in Fig. 2b and c. For the reasons evoked in the method section, it was not possible to have a continuous monitoring of the points (Pts) and several curves are interrupted. Also, there was a total interruption during the 2012–2013 winter. The figure then shows two distinct campaigns of measurements (squares and circles in Fig. 2a) due to a reset of the targets and reference locations. The first campaign (Fig. 2b) started directly after the event of August 2010 and the second (Fig. 2c) in May 2013. A first comparison of the two data sets shows that mean velocities measured during the 2013–2016 period are on average lower than during the 2010–2012 period (compare Fig. 2b and c). The velocity field (Fig. 2a) does not reveal significant spatial changes and the two data sets are interpreted conjointly according to the zone activity.

A first group of 8 targets was installed in the erosion zone EZ (upper part of the landslide; Fig. 2a): Pts 1 and 2 in the vicinity of the main headscarp, Pt 3 in the centre of the upper part, Pt5 just over the main secondary scarp (MSS) and Pts 8 to 11 on the eastern lateral spur. All these points underwent weak motions with a velocity lower than 0.8 m per year (Fig. 2b and c). In contrast, the three targets installed just below MSS (Pts 4, 6 and 7) exhibit higher mean velocities (> 1.5 m/year). This is particularly the case of Pt7, where mean and maximum velocities reached 5 and 16 m/year, respectively (Fig. 2a). These results, which reveal an activity higher at the secondary headscarp than at the main one since 2010, differ from the observation prior to 2010 showing that the main headscarp was significantly more active (Jaboyedoff et al., 2009). Below the MSS, Pt 13 (that replaced Pt 12) and Pt 14 were installed in an active gullying sector (Fig. 2a), on small crests between which the material was flowing superficially. The measured mean velocities (between 1 and 2.6 m/year) then give a minimum value of the velocity. Further down the slope, the targets located in the transportation zone TZ (Pts 15, 16, 18, 19, 20, 21, 22, 23 and 24; Fig. 2a) exhibit the highest average velocities, ranging from 2.3 to 7.2 m/year (Fig. 2b and c), with maxima reaching 8.3 m/year (Fig. 2a and c). TZ then appears to be the most active area in the landslide at the time of the survey. No target was installed in the accumulation zone AZ and the activity in this area will be analysed using TLS results (see next section).

To summarize, the landslide behaviour during the survey period was characterized by a relatively high activity in the translational zone with a mean velocity of about 3.5 m/year, and maximum velocities as high as 12 m/year. This zone is affected by superficial erosion and the eroded materials are transported to feed the downhill accumulation zone. In contrast, the erosion zone EZ above the main secondary scarp appears now little active with a mean velocity lower than 0.8 m/year.

4.2. Terrestrial laser scanning

The TLS surveys provide an insight of the general behaviour of the PBL and the results are presented in Fig. 3. The upper part (EZ) shows little change between 2011 and 2016, except some small erosional pattern. The main secondary scarp MSS shows positive differences (+1 m, yellow to orange colours in Fig. 3) which, in this case, is the expression of a limited “toppling” of rock compartments due to the opening of cracks at the crest. Directly below this latter, superficial deposition occurs. In the main gully and on its side, the negative difference (−1 m, light-blueish in Fig. 3) indicates erosional processes. This is followed downward by extended negative change (−2 to −2.5 m) which indicates a loss in altitude in the transportation zone TZ, where large local bulges are moving down. Finally, at the toe of the landslide, a positive difference is observed (up to +2.5 m, yellow to red colours in Fig. 3). This corresponds to the accumulation zone AZ, where materials originating from the transportation zone are stocked. The aforementioned deformation behaviour, detected from both target tracking and from differential TLS DEM analysis, is in good agreement with movement patterns that developed before 2010 (Mainsant et al., 2012a).

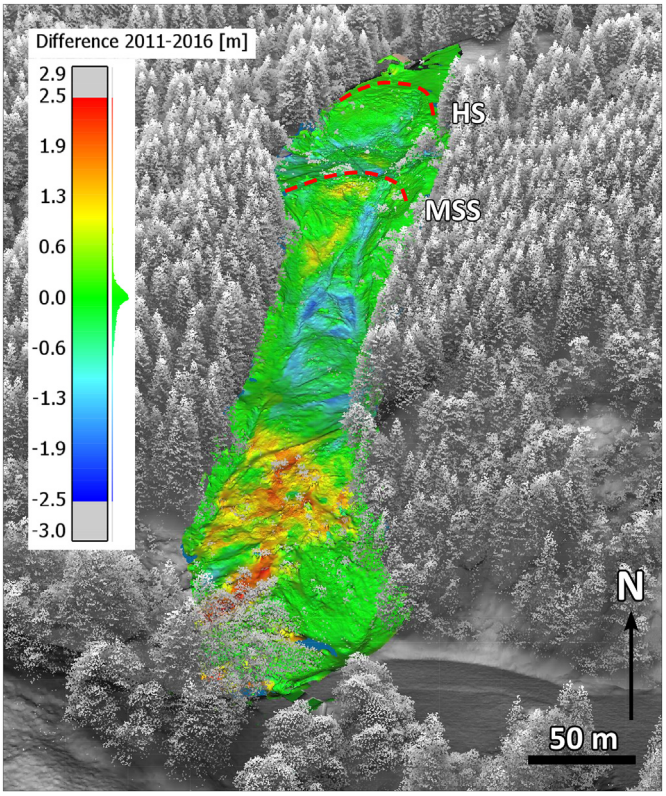

Fig. 3. Comparison between TLS point clouds of April 2011 and May 2016 draped on HRDEM. The difference obtained by the closest point distance method shows the general deformation of the Pont-Bourquin Landslide (PBL). The scale is in metres and the positive values show an accumulation while the negative one shows a subsidence. The most notable aspects are the loss of material in the centre part (up to −2.5 m) and the bulging at the toe (up to 2 m). HS: headscarp; MSS: main secondary scarp.

4.3. Environmental and seismic monitoring

Correlograms of the three pairs of stations are presented in Fig. 4 along with their average (reference) correlogram, in white. Fig. 4a depicts the seismic correlograms of pair 1a-1b between early March 2010 and mid-March 2016. Note that no data were recorded between 21 August 2010 and 25 October 2011. *dV/V* data from 2010 are from Mainsant et al. (2012a) and were filtered in the frequency range 10–12 Hz. Data starting from late 2011 up to mid-March 2016 are original and were band-pass filtered between 8 and 12 Hz. According to Weaver et al. (2011), a wider frequency bandwidth (8–12 Hz) was used to reduce *dV/V* measurement errors. Daily correlograms are slightly asymmetric in the central part, which indicates that noise sources are not homogeneously spread around the seismic sensors for these short times. This confirms the predominant role of the traffic on the road at the toe of the landslide as a source of energy. To avoid the instability of the first arrivals due to slight changes in source occurrences, a time window in the range -2 s to −0.2 s and + 0.2 s to +2 s (indicated by vertical dashed lines in Fig. 4) was used.

From these daily correlograms and the reference correlogram, daily *dV/V* values were computed. Fig. 5a presents the temporal evolution of *dV/V* for pair 1a-1b, along with the correlation coefficient *cc* between the daily correlogram and the reference correlogram in Fig. 5b. The *dV/V* (resp. *cc*) time-series exhibit variations between −2% and + 2% (resp. 0.6 and 0.95) over the recording period. The first key point in this figure is that the only drop below −2% and down to around −6% ($cc < 0.6$) is preliminary to the earthflow which occurred on 19 August 2010. Moreover, it can be observed that the drop in *dV/V* below −2% started up to one week before the flow. A complete description and analysis of this flow event in relation to the *dV/V* drop can be found in Mainsant et al. (2012a).

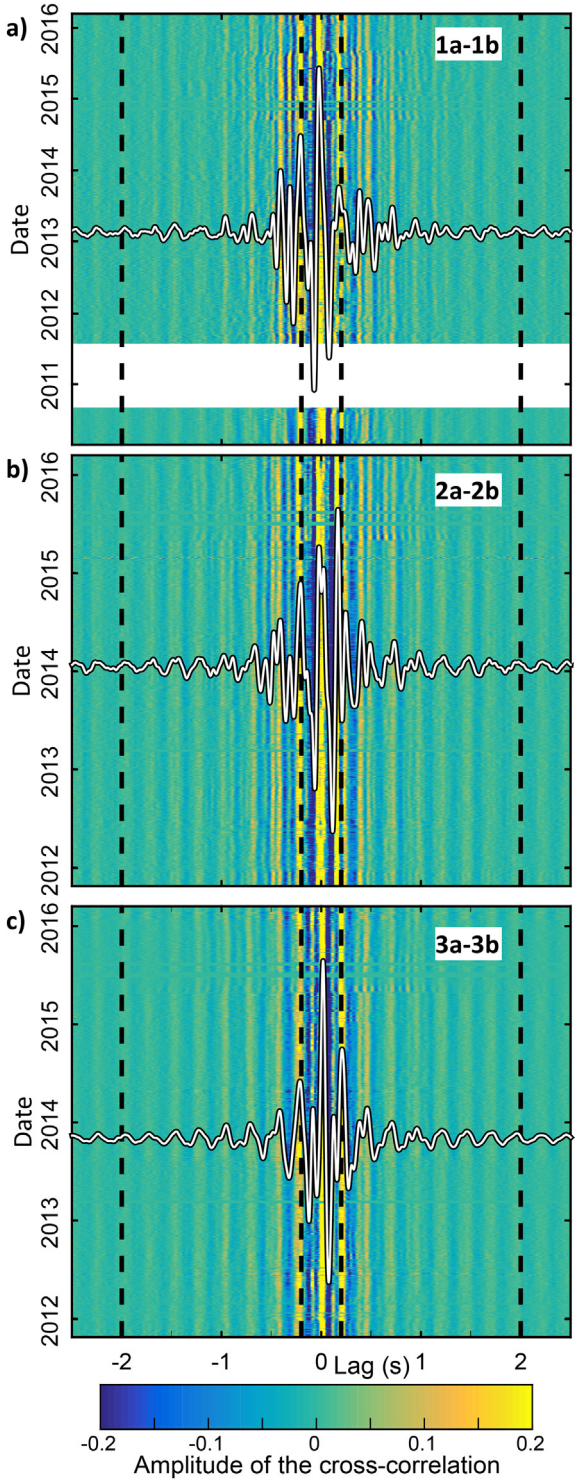

Fig. 4. a), b) and c) Temporal evolution of daily correlograms of pairs 1a-1b, 2a-2b and 3a-3b, respectively, between 25 October 2011 and 15 March 2016. The colour scale refers to the amplitude of the cross-correlation. The white wavelet corresponds to the average correlogram. Vertical dashed lines stand for the time limits used for the computation of *dV/V* between [−2 s −0,2 s] and [0.2 s 2 s].

The second key point in Fig. 5 is that, since 2010, no *dV/V* value below −2% is observed. This is concomitant with the fact that no catastrophic landslide acceleration occurred during this period.

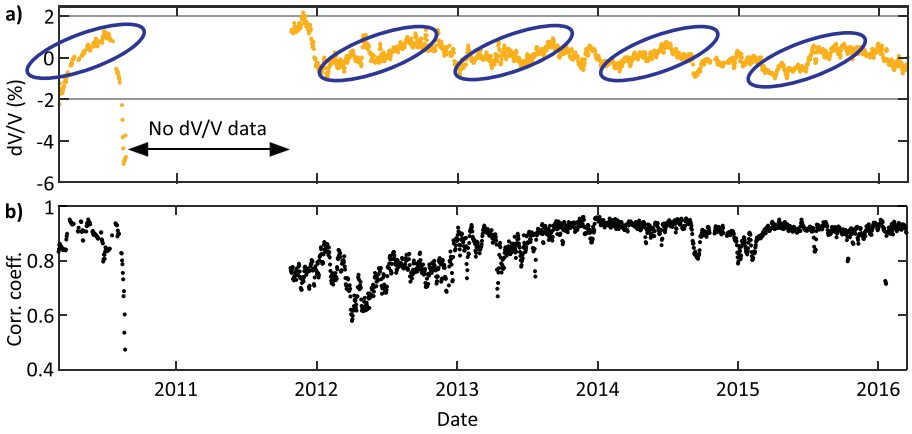

Fig. 5. a) Relative velocity changes *dV/V* for pair 1a-1b between March 2010 and March 2016, for the frequency range 8–12 Hz. The horizontal grey lines represent the limit of *dV/V* between −2 and + 2%. b) The associated correlation coefficient. Data between 01 March 2010 and late August 2010 are from Mainsant et al. (2012a).

Concerning the observed variations in the range ± 2%, it is worth noting that they are not scattered. On the contrary, they present patterns marked by repetitive seasonal fluctuations (blue ellipses in Fig. 5a), suggesting a control of *dV/V* time-series fluctuations by meteorological parameters. To further investigate this issue, seismic data from the three pairs of sensors (1a-1b to 3a-3b) were cross-correlated and *dV/V* time-series were derived from each pair in the frequency range 8–12 Hz. As for pair 1a-1b, daily correlograms for pairs 2a-2b and 3a-3b are shown in Fig. 4b and c, respectively, along with their corresponding average correlogram.

Fig. 6 shows the data used to study the relationship between seismic velocity changes and environmental and displacement variables. The computed *dV/V* values for the three pairs of sensors are presented in Fig. 6a. The three seismic velocity curves exhibit the same trend. As for pair 1a-1b, no relative velocity drop below −2% (or increase above +2%) is observed for the other pairs during the monitored period. The three time-series present gentle, relatively regular and parallel

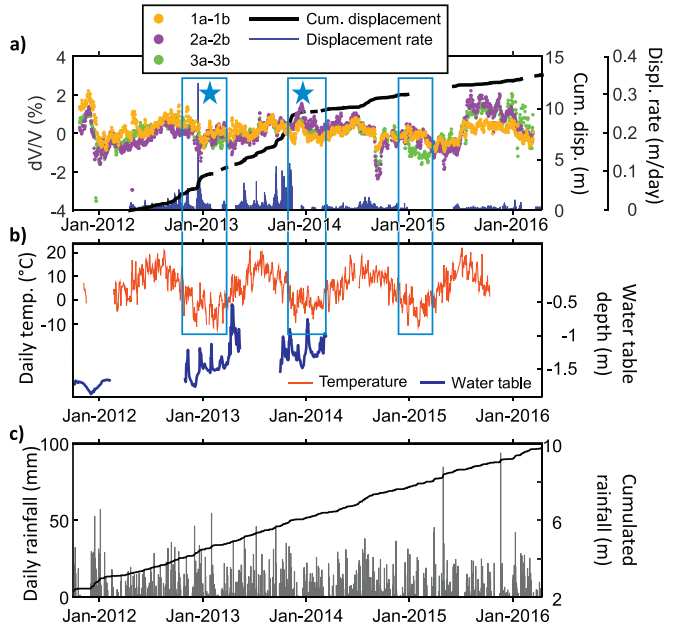

Fig. 6. Seismic, kinematics and environmental time-series. a) Seismic velocity (dots) derived from the three pairs of sensors (1a-1b, 2a-2b, and 3a-3b) and extensometer data (black line and blue bars). The two blue stars denote the two *dV/V* peaks that could result from icing effect during the main freezing periods (blue rectangles) b) Water table (blue curve) and daily temperature (red curve). c) Daily rainfall (grey bars) and cumulated rainfall (black curve). (For interpretation of the references to colour in this figure legend, the reader is referred to the web version of this article.)

variations. This suggests that, in first approach, *dV/V* between the three pairs of sensors are globally sensitive to the same controlling factors and react more or less similarly and simultaneously at the scale of the landslide. Fig. 6a also presents extensometer data (see location in Fig. 1a) under the form of daily and cumulative displacements. The discontinuity of the curve indicates that no data were recorded at several intervals, resulting in a total number of available daily measurements of 1248 for a monitoring period of 1458 days. The curve globally exhibits regular trends with average motions of 9 mm/day in 2012, 12.5 mm/day in 2013, 2.5 mm/day from late 2013 to July 2014 and 4 mm/day from September 2014 to May 2016. Three main (but limited) acceleration phases can be observed. The first occurred from mid- to late-December 2012 with an average velocity of 52.5 mm/day and a peak velocity of 330 mm/day on December 17. The second acceleration is observed from mid-October 2013 to mid-November 2013 (average velocity of 60 mm/day) and the third, with a lower average motion (16 mm/day), took place from mid-July 2014 to late August 2014. Environmental data are shown in Fig. 6b (temperature and water table) and in Fig. 6c (daily and cumulated rainfall). The distribution of rainfall appears relatively regular over the studied period, while the water table (blue curve in Fig. 6b) was located between 2 m and 0.5 m below the surface (location of the piezometer in Fig. 1a). Piezometric data show rapid rises of several tens of cm after rainfall, followed by slow decreases. The dataset is however truncated (432 days with data over the 1458 days-long recording period) and does not provide a full seasonal cycle. This dataset will not be used in the following cross-correlation study.

Finally, the temperature dataset (red curve in Fig. 6b) exhibits a classical main period of one year, with values between −10 °C and + 20 °C. Because temperatures are averaged over one day, the 24 h-long cycles cannot be evidenced.

The relation between displacement rates (extensometer data) and the environmental parameters (rainfall and air temperature) was first studied by cross-correlating the time-series. The two cross-correlation curves are shown in Fig. 7a, where the grey stripe represents the confidence interval of 95% (Eq. (1)). The correlogram displacement rate/rainfall (black curve) shows a positive correlation with a 2-day long peak starting at a positive lag of about 1 day and a limited significance (*cc* of around 0.15). This suggests that displacements measured by the extensometer are initiated shortly (maximum of 1 day) after a rain event. The further decrease of *cc* furthermore indicates that rainfall has no more significant effect on surface displacements around two weeks after rain events (*cc* values within the 95% confidence interval). However, the daily time series do not allow to accurately determine the reaction times and hourly measurements would be required to achieve a better temporal resolution. A weak positive cross-correlation (*cc* = 0.24) was found between displacement rate and air temperature (filtered to keep only periods higher than 300 days), with a lag of about

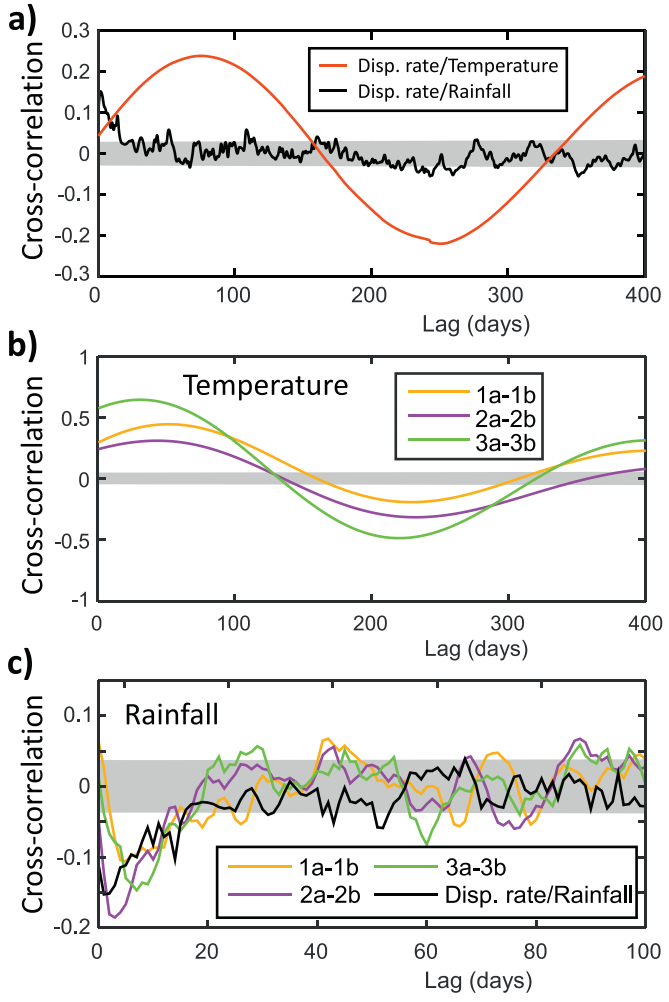

Fig. 7. Cross-correlation results. The grey stripe stands for values within the 95% confidence interval. a) Cross-correlation between displacement rates (extensometer data) and rainfall (black curve) series, and between displacement rates and air temperature series, filtered to keep periods higher than 300 days (red curve). b) Cross-correlation between *dV/V* and air temperature time series filtered for periods higher than 300 days. c) Cross-correlation between *dV/V* and rainfall for the three pairs of sensors (1a-1b to 3a-3b). Time series are filtered for periods lower than 90 days. The black curve corresponds to the inverse cross-correlation of displacement rate with rainfall data (black curve in Fig. 7a). (For interpretation of the references to colour in this figure legend, the reader is referred to the web version of this article.)

60–90 days (Fig. 7a, red curve). Looking at the time series (Fig. 6), this amazing result probably originates from the occurrence of two acceleration phases at almost the same periods (late autumn) in 2012 and 2013, but not in 2014. Our interpretation is that this coincidence over two years generated this apparent correlation.

To study the dependency of seismic velocity changes to environmental parameters, *dV/V* data were cross-correlated with air temperature for the three pairs of sensors (Fig. 7b). Time series were low-pass filtered with a period of 300 days to highlight seasonal cycles. Positive and significant peaks are observed at lags of around 30 days (3a-3b; $cc = 0.64$), 40 days (2a-2b; $cc = 0.32$) and 50 days (1a-1b; $cc = 0.44$). The positive correlation of *dV/V* and temperature data indicates that an increase (resp. a decrease) of temperature increases (resp. decreases) the rigidity of the clayey material, probably due to drying and decrease in soil moisture (Mainsant et al., 2012b). The different delays observed in Fig. 7b suggest that *dV/V* variations are not synchronous at the scale of the landslide. *dV/V* at the top of the slide (pair 3a-3b) reacts quicker to temperature (around 30 days) than the two other pairs of sensors (around 40 to 50 days). This could result from the presence of numerous cracks observed in the zone below the main secondary scarp (Fig. 1c), favouring the penetration of the heat front at depth. For the lowest temperatures (in winter), *dV/V* tends to decrease or is close to its minimum value (Fig. 6a). During freezing periods (blue rectangles in Fig. 6), *Vs* could increase in the shallow layer, due to ice formation. This effect could, however, be tempered by the presence of a thermally isolating snow layer. Two small positive *dV/V* peaks (shown by stars in Fig. 6a) are observed during freezing periods, suggesting a potential but limited effect of icing.

The cross-correlation curves between seismic velocity variations and rainfall for the three sensor pairs (Fig. 7c) have an irregular shape and exhibit weak negative peaks ($cc < 0.2$) located at lags of 2 days (2a-2b), 5 days (1a-1b) and around 7 days (3a-3b). This anti-correlation suggests that rainfall, and subsequent water infiltration within the ground, could induce a decrease in surface wave seismic velocity. Following the peaks, *cc* increases linearly and regularly up to a non-significant level for lags over around 20 days. The cross-correlation between displacement rate (extensometer) and rainfall data (presented in Fig. 7a) is superimposed on curves in Fig. 7c, with *cc* values multiplied by -1 for comparison. Curves do match and show identical shapes, with a slightly larger lag observed for the *dV/V* response (> 2 days) compared to the displacement rate curve (about one day). The low *cc* values, however, indicate that the rainfall effect on *dV/V* is not of prime importance, in contrast to the temperature influence. The weak correlation and the curve irregularity also make it difficult to draw firm conclusions on the lag values.

5. Discussion

Surface displacements monitoring from point targets and TLS data showed that the PBL can be divided into three main deformation units. The upper part (EZ) shows moderate motion (between 0 and 1.5 m/year; Figs. 2 and 3). This zone is mainly affected by erosion, toppling and fracture opening phenomena, which result in a loss of materials. The central part located below the MSS exhibits higher motions (1.5 to 5 m/year; Figs. 2 and 3) and consists principally in the transportation of the upper eroded materials (TZ: Transportation Zone). Finally, the zone located at the bottom of the PBL is the previously defined accumulation zone AZ (Figs. 2 and 3) where a bulge is forming. The three pairs of seismic sensors 1a-1b to 3a-3b are located to investigate the upper part of the transportation zone (below the MSS), in the middle of the transportation zone where the displacement rates are the highest, and at the top of the accumulation zone.

5.1. Influence of environmental parameters on dV/V

The cross-correlation of the *dV/V* data with environmental data has shown a significant influence of the temperature on the seismic velocity variations in the 8–12 Hz range at the seasonal scale (Fig. 7b), with a delay varying between about 30 to 50 days. These relatively low lag values indicate an influence of the shallow layers on the *dV/V* variations. A simple computation was performed using a 1D heat conduction equation, similar to that performed by Bottelin et al. (2013a), using a thermal diffusivity $D = 5 \times 10^{-7}\,m^2.\ s^{-1}$ for the clayey material (Krzeminska et al., 2012). Computations show that the heat front after 30 and 50 days is located at about 1.2 and 2 m in depth, respectively. Temperature would increase the ground rigidity through a decrease in water content and subsequent shrink effects. This interpretation is supported by controlled laboratory experiments on clays (Mainsant et al., 2012b) that pointed out that a decrease (resp. increase) in moisture results in a decrease (resp. increase) in *Vs*. The shorter delay (30 days) observed for the sensor pair 3a-3b could be related to the numerous cracks observed in the upper part of the transportation zone below the MSS (Fig. 1c), favouring penetration of the heat wave. This thermal effect on the *dV/V* variations in the superficial layers is in

agreement with depth sensitivity kernels conducted by Mainsant et al. (2012a), who showed that the surface wave velocity in the frequency range 8–12 Hz is affected both by superficial (in the first two metres) and by deeper (around 10 m depth) changes in *Vs* properties. The short measured delay values clearly indicate that seasonal *dV/V* variations are controlled by thermal induced changes in rigidity in the shallow layer.

In the short term, our study also reveals that rainfall could have a weak influence on the shallow rigidity variations, with a low negative correlation (less significant than the one observed for temperature) between rainfall and *dV/V* variations and delays varying between 2 and 7 days (Fig. 7c). Such low correlation is also observed between displacement rate data (provided by the extensometer located in the middle of the transportation zone) and rainfall data (Fig. 7a), with however a shorter delay of about 1 day and in-phase variation. This slight difference in delay could originate from the different sensing depths of the measurements. While the extensometer measures superficial deformation, *dV/V* calculated in the frequency range of 8–12 Hz is sensitive to the first two metres, as mentioned before. The observed differential lags might then be indicative of the delay corresponding to the time needed for rainfall to infiltrate and influence the rigidity.

5.2. Slope response to environmental parameters and deformation mechanism

The slope structure is sketched in Fig. 8a with the four layers L1 to L4 identified from seismic prospecting (see Fig. 1c). The 2 m-thick upper layer (L1) is characterized by a very low rigidity (*Vs* = 90 m/s) and a high degree of fracturing explaining the presence of a shallow water table. The more rigid underlying layer L2 (*Vs* = 360 m/s) is about 9 m thick and slides over the bedrock (L4; *Vs* = 640 m/s). During the 2010 earthflow, the 6% drop in *dV/V* was interpreted as a decrease in *Vs* (from 360 m/s to 200 m/s) in a 2 m thick layer at the base of the landslide (L3 in Fig. 8a).

The cross-correlation analysis between the weak reversible *dV/V* variations (−2%, +2%) and the environmental parameters showed relatively short delays that suggest a predominant control and response of the 2 m thick upper layer. On the other hand, the medium to low correlation coefficients obtained when cross-correlating *dV/V* with air temperature (*cc* = 0.5) and rainfall (*cc* = 0.24) indicate the probable influence of other factors on *dV/V* fluctuations. Indeed, this shallow layer is strongly exposed to numerous phenomena likely to change *Vs*, such as temperature and moisture fluctuations, water level changes, ice formation and fissure opening and closing. The full understanding of *dV/V* variations would require the acquisition of a long and complete time series of the water table, snow thickness, and also soil temperature and moisture at different depths.

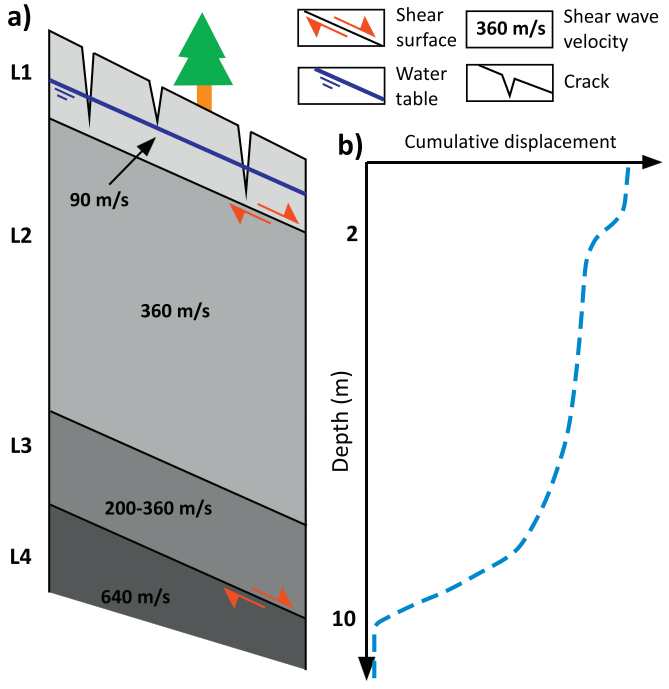

Fig. 8. Sketch showing the slope deformation mechanism. a) The soil column with the 4 layers (L1 to L4) defined from seismic prospecting (see Fig. 1c) and *Vs* values in each layer. b) the hypothesized cumulative displacement profile.

Extensometer data (Fig. 7a) reveal a slight response time to rainfall < 24 h in the transportation zone, while cumulative rainfall (more than two days) has little to no effect on the landslide kinematics. This quick response in terms of slide velocity to rainfalls suggests the presence of a shallow rupture surface at the base of the shallow layer L1, in addition to the main surface rupture already identified at the top of the bedrock (Fig. 8a; Mainsant et al., 2012a). The mechanism of the landslide could then be illustrated by the hypothesized inclinometer profile shown in Fig. 8b, where the displacement rate measured at the surface is mainly partitioned in two zones located at about 2 m and 10 m depth. The partitioning degree between the two rupture surfaces still remains unknown because of the lack of data at depth and the difficulty to keep a borehole in operation longer than a few weeks or months (Mainsant et al., 2012a). In this respect, *dV/V* measurements could offer an alternative in getting information on rigidity variations in the landslide mass.

6. Conclusions

Following the occurrence of an earthflow/mudflow of a few thousand cubic metres at the toe of the Pont-Bourquin Landslide (Swiss Alps) in late August 2010 and the sharp drop of 6% in d*V/V* that was measured up to seven days before that event, a seismic monitoring system made of three pairs of sensors was installed across the transportation and accumulation zones of the landslide. The seismic monitoring system allowed daily relative changes in seismic velocity to be measured for a period of 4.5 years between late October 2011 and mid-March 2016. No dramatic drop of the seismic velocity was observed during this period, consistently with the lack of significant landslide acceleration or earthflow/mudflow events. Slow motion however occurred, as shown by the geodetic target tracking (slide velocity of 1 to 5 m/yr) and the elevation variations in the transportation and accumulation zones, reaching −2.5 m and 2.5 m in 4.5 years, respectively. During the quiet period after the August 2010 event, the seismic velocity time series show periodic and reversible variations in a range − 2% to +2%, suggesting a probable influence of seasonal parameters.

The three seismic time series were cross-correlated with daily environmental data (rainfall, temperature). In the long term (yearly scale), d*V/V* variations are mainly driven by the temperature with relatively short delays varying from 30 days below the main secondary scarp (*MSS*) to 50 days at the top of the accumulation zone. These lag values indicate that the shallow layer (2 m or less) controls the d*V/V* variations, explaining the faster response in the fractured zone just below the *MSS*. In the short term, the rigidity variations (measured by the parameter *dV/V*) are weakly correlated to rainfall, exhibiting a small decrease in *dV/V* with a delay of a few days.

Although no acceleration and fluid-like motion occurred during the studied period, the continuous monitoring of *dV/V* has proved to be a robust method for getting information at depth, with no data gap even in snow conditions, in contrast to extensometer data. The seasonal reversible seismic velocity variations turned out to be in a range lower than the drop observed before the August 2010 earthflow/mudflow, highlighting the interest of incorporating the *dV/V* technique in monitoring systems.

Acknowledgements

Grégory Bièvre, Eric Larose and Denis Jongmans (ISTerre) are part of LabEx OSUG@2020 (ANR10604 LABX56). This work received additional funding from the VOR program (Université Grenoble Alpes). We thank our colleagues at UNIL: Marc-Henri Derron, Cédric Meier and Clément Michoud for their support in the field and previous studies. The authors thank two anonymous reviewers and the editor who greatly helped to enhance the quality of this manuscript.

Appendix A. Supplementary data

Supplementary data to this article can be found online at https://doi.org/10.1016/j.enggeo.2018.08.013.

References

Arnone, E., Noto, L., Lepore, C., Bras, R., 2011. Physically-based and distributed approach to analyze rainfall-triggered landslides at watershed scale. Geomorphology 133, 121–131. https://doi.org/10.1016/j.geomorph.2011.03.019.

Badoux, H., Gabus, J.H., Mercanton, C.H., 1990. Les Diablerets, scale 1:25000. In: Swiss Geological Atlas, Sheet. Swiss Federal Office for Water and Geology, Wabern, Switzerland, pp. 1285.

Bonnefoy-Claudet, S., Cotton, F., Bard, P.Y., 2006. The nature of noise wavefield and its applications for site effects studies: a literature review. Earth Sci. Rev. 79 (3–4), 205–227.

Bottelin, P., Jongmans, D., Baillet, L., Lebourg, T., Hantz, D., Lévy, C., Le Roux, O., Cadet, H., Lorier, L., Rouiller, J.-D., Turpin, J., Darras, L., 2013a. Spectral analysis of prone-to-fall rock compartments using ambient vibrations. J. Environ. Eng. Geophys. 18, 205–217. https://doi.org/10.2113/JEEG18.4.205.

Bottelin, P., Lévy, C., Baillet, L., Jongmans, D., Guéguen, P., 2013b. Modal and thermal analysis of Les Arches unstable rock column (Vercors massif, French Alps). Geophys. J. Int. 194, 849–858. https://doi.org/10.1093/gji/ggt046.

Bottelin, P., Baillet, L., Larose, E., Jongmans, D., Hantz, D., Brenguier, O., Cadet, H., Helmstetter, A., 2017. Monitoring rock reinforcement works with ambient vibrations: La Bourne case study (Vercors, France). Eng. Geol. 226, 136–145. https://doi.org/10.1016/j.enggeo.2017.06.002.

Brönnimann, C., 2011. Effect of Groundwater on Landslide Triggering. PhD Thesis. École Polytechnique Fédérale de Lausanne, Switzerland.

Burjánek, J., Gassner-Stamm, G., Poggi, V., Moore, J.R., Fäh, D., 2010. Ambient vibration analysis of an unstable mountain slope. Geophys. J. Int. 180, 820–828. https://doi.org/10.1111/j.1365-246X.2009.04451.x.

Burjánek, J., Moore, J.R., Yugsi Molina, F.X., Fäh, D., 2012. Instrumental evidence of normal mode rock slope vibration. Geophys. J. Int. 188, 559–569. https://doi.org/10.1111/j.1365-246X.2011.05272.x.

Burjánek, J., Gischig, V., Moore, J.R., Fäh, D., 2018. Ambient vibration characterization and monitoring of a rock slope close to collapse. Geophys. J. Int. 212, 297–310. https://doi.org/10.1093/gji/ggx424.

Chatfield, C., 2003. The Analysis of Time Series: An Introduction. Chapman & Hall/CRC Press, London, England.

Colombero, C., Baillet, L., Comina, C., Jongmans, D., Vinciguerra, S., 2017. Characterization of the 3-D fracture setting of an unstable rock mass: from surface and seismic investigations to numerical modeling. J. Geophys. Res. 122, 6346–6366. https://doi.org/10.1002/2017JB014111.

Del Gaudio, V., Muscillo, S., Wasowski, J., 2014. What we can learn about slope response to earthquakes from ambient noise analysis: an overview. Eng. Geol. 182, 182–200. https://doi.org/10.1016/j.enggeo.2014.05.010.

Diggle, P.D., 1990. Time series: a biostatistical Introduction. Oxford Statistical Science Series Vol. 5, Oxford Science Publications, Oxford, England.

Fan, L., Lehmann, P., Or, D., 2015. Effects of hydromechanical loading history and antecedent soil mechanical damage on shallow landslide triggering. J. Geophys. Res. 120, 1990–2015. https://doi.org/10.1002/2015JF003615.

Franz, M., Carrea, D., Abellán, A., Derron, M.-H., Jaboyedoff, M., 2016. Use of targets to track 3D displacements in highly vegetated areas affected by landslides. Landslides 13, 821–831. https://doi.org/10.1007/s10346-016-0685-7.

Glade, T., Crozier, M., Smith, P., 2000. Applying probability determination to refine landslide-triggering rainfall thresholds using an empirical Antecedent Daily Rainfall Model. Pure Appl. Geophys. 157, 1059–1079. https://doi.org/10.1007/s000240050017.

Guzzetti, F., 2000. Landslide fatalities and the evaluation of landslide risk in Italy. Eng. Geol. 58, 89–107. https://doi.org/10.1016/S0013-7952(00)00047-8.

Hadziioannou, C., Larose, E., Coutant, O., Roux, P., Campillo, M., 2009. Stability of monitoring weak changes in multiply scattering media with ambient noise correlation: Laboratory experiments. J. Acoust. Soc. Am. 125, 3688–3695. https://doi.org/10.1121/1.3125345.

Helmstetter, A., Garambois, S., 2010. Seismic monitoring of Séchilienne rockslide (French Alps): Analysis of seismic signals and their correlation with rainfalls. J. Geophys. Res. 115, F03016. https://doi.org/10.1029/2009JF001532.

Hungr, O., Leroueil, S., Picarelli, L., 2014. The Varnes classification of landslide types, an update. Landslides 11, 167–194. https://doi.org/10.1007/s10346-013-0436-y.

Iverson, R.M., Reid, M.E., Iverson, N.R., Lahusen, R.G., Logan, M., Mann, J.E., Brien, D.L., 2000. Acute sensitivity of landslide rates to initial soil porosity. Science 290, 513–516. https://doi.org/10.1126/science.290.5491.513.

Jaboyedoff, M., Pedrazzini, A., Loye, A., Oppikofer, T., Güell, I., Pons, M., Locat, J., 2009. Earth Flow in a Complex Geological Environment: The Example of Pont Bourquin, Les Diablerets (Western Switzerland). In: Malet, J.-P., Remaître, A., Bogaard, T.A. (Eds.), Landslide Processes, from Geomorphologic Mapping to Dynamic Modelling. CERG Edition, Strasbourg, France.

Jongmans, D., Bièvre, G., Schwartz, S., Renalier, F., Beaurez, N., 2009. Geophysical investigation of the large Avignonet landslide in glaciolacustrine clays in the Trièves area (French Alps). Eng. Geol. 109, 45–56. https://doi.org/10.1016/j.enggeo.2008.10.005.

Krzeminska, D.M., Steele-Dunne, S.C., Bogaard, T.A., Rutten, M.M., Sailhac, P., Geraud, Y., 2012. High-resolution temperature observations to monitor soil thermal properties as a proxy for soil moisture condition in clay-shale landslide. Hydrol. Process. 26, 2143–2156. https://doi.org/10.1002/hyp.7980.

Larocque, M., Mangin, A., Razack, M., Banton, O., 1998. Contribution of correlation and spectral analyses to the regional study of a large karst aquifer (Charente, France). J. Hydrol. 205, 217–231. https://doi.org/10.1016/S0022-1694(97)00155-8.

Larose, E., Carrière, S., Voisin, C., Bottelin, P., Baillet, L., Guéguen, P., Walter, F., Jongmans, D., Guillier, B., Garambois, S., Gimbert, F., Massey, C., 2015. Environmental seismology: what can we learn on earth surface processes with ambient noise? J. Appl. Geophys. 116, 62–74. https://doi.org/10.1016/j.jappgeo.2015.02.001.

Lee, J.-Y., Lee, K.-K., 2000. Use of hydrologic time series data for identification of recharge mechanism in a fractured bedrock aquifer system. J. Hydrol. 229, 190–201. https://doi.org/10.1016/S0022-1694(00)00158-X.

Lee, L., Lawrence, D., Price, M., 2006. Analysis of water-level response to rainfall and implications for recharge pathways in the Chalk aquifer, SE England. J. Hydrol. 330, 604–620. https://doi.org/10.1016/j.jhydrol.2006.04.025.

Lévy, C., Baillet, L., Jongmans, D., Mourot, P., Hantz, D., 2010. Dynamic response of the Chamousset rock column (Western Alps, France). J. Geophys. Res. 115. https://doi.org/10.1029/2009JF001606.

Lu, N., Godt, J.W., Wu, D.T., 2010. A closed-form equation for effective stress in unsaturated soil. Water Resour. Res. 46, W05515. https://doi.org/10.1029/2009WR008646.

Mainsant, G., Larose, E., Brönnimann, C., Jongmans, D., Michoud, C., Jaboyedoff, M., 2012a. Ambient seismic noise monitoring of a clay landslide: toward failure prediction. J. Geophys. Res. 117, F01030. https://doi.org/10.1029/2011JF002159.

Mainsant, G., Jongmans, D., Chambon, G., Larose, E., Baillet, L., 2012b. Shear-wave velocity as an indicator for rheological changes in clay materials: Lessons from laboratory experiments. Geophys. Res. Lett. 39, L19301. https://doi.org/10.1029/2012GL053159.

Malet, J.-P., Laigle, D., Remaître, A., Maquaire, O., 2005. Triggering conditions and mobility of debris flows associated to complex earthflows. Geomorphology 66, 215–235. https://doi.org/10.1016/j.geomorph.2004.09.014.

Méric, O., Garambois, S., Malet, J.-P., Cadet, H., Guéguen, P., Jongmans, D., 2007. Seismic noise-based methods for soft-rock landslide characterization. Bulletin de la Societé Géologique de France 178, 137–148.

Okkonen, J., Klove, B., 2010. A conceptual and statistical approach for the analysis of climate impact on ground water table fluctuation patterns in cold conditions. J. Hydrol. 388, 1–12. https://doi.org/10.1016/j.jhydrol.2010.02.015.

Petley, D.N., 2004. The evolution of slope failures: mechanisms of rupture propagation. Nat. Hazards Earth Syst. Sci. 4, 147–152. https://doi.org/10.5194/nhess-4-147-2004.

Picarelli, L., Urciuoli, G., Russo, C., 2004. Effect of groundwater regime on behaviour of clayey slopes. Can. Geotech. J. 41, 467–484. https://doi.org/10.1139/t04-009.

Renalier, F., Bièvre, G., Jongmans, D., Campillo, M., Bard, P.-Y., 2010a. Characterization and monitoring of unstable clay slopes using active and passive shear wave velocity measurements. In: Miller, R.D., Bradford, J.D., Holliger, K. (Eds.), Advances in Near-Surface Seismology and Ground-Penetrating Radar. Society of Exploration Geophysics, Tulsa, USA. https://doi.org/10.1190/1.9781560802259.ch24.

Renalier, F., Jongmans, D., Campillo, M., Bard, P.-Y., 2010b. Shear wave velocity imaging of the Avignonet landslide (France) using ambient noise cross-correlation. J. Geophys. Res. 115, F03032. https://doi.org/10.1029/2009JF001538.

Rusinkiewicz, S., Levoy, M., 2001. Efficient Variants of the ICP Algorithm. pp. 145–152.

Salvi, J., Matabosch, C., Fofi, D., Forest, J., 2007. A review of recent range image registration methods with accuracy evaluation. Image Vis. Comput. 25, 578–596. https://doi.org/10.1016/j.imavis.2006.05.012.

Sens-Schönfelder, C., Wegler, U., 2006. Passive image interferometry and seasonal variations of seismic velocities at Merapi Volcano, Indonesia. Geophys. Res. Lett. 33, L21302. https://doi.org/10.1029/2006GL027797.

Shapiro, N.M., Campillo, M., 2004. Emergence of broadband Rayleigh waves from correlations of the ambient seismic noise. Geophys. Res. Lett. 31, L07614. https://doi.org/10.1029/2004GL019491.

Simoni, S., Zanotti, F., Bertoldi, G., Rigon, R., 2008. Modelling the probability of occurrence of shallow landslides and channelized debris flows using GEOtop-FS. Hydrol. Process. 22, 532–545. https://doi.org/10.1002/hyp.6886.

Snieder, R., Larose, E., 2013. Extracting Earth's Elastic Wave Response from Noise Measurements. Annu. Rev. Earth Planet. Sci. 41, 183–206. https://doi.org/10.1146/annurev-earth-050212-123936.

Valentin, J., Capron, A., Jongmans, D., Baillet, L., Bottelin, P., Donze, F., Larose, E., Mangeney, A., 2017. The dynamic response of prone-to-fall columns to ambient vibrations: comparison between measurements and numerical modelling. Geophys. J. Int. 208, 1058–1076. https://doi.org/10.1093/gji/ggw440.

von Ruette, J., Papritz, A., Lehmann, P., Rickli, C., Or, D., 2011. Spatial statistical modeling of shallow landslides—Validating predictions for different landslide inventories and rainfall events. Geomorphology 133, 11–22. https://doi.org/10.1016/j.geomorph.2011.06.010.

Weaver, R.L., Hadziioannou, C., Larose, E., Campillo, M., 2011. On the precision of noise correlation interferometry. Geophys. J. Int. 185, 1384–1392. https://doi.org/10.1111/j.1365-246X.2011.05015.x.